Creep-Driven Solute Segregation to Planar Faults in Ni-Base Single-Crystal Superalloys

ZHONGMIN LONG , DAVID BÜRGER , LUKAS GRÜNEWALD , VAMSHI KRISHNA RAO, K.V. VAMSI, and YOLITA M. EGGELER

This study proposes that creep-induced segregation to planar faults reflects the dynamic establishment of a new compositional steady state within the two-phase γ/γ' single-crystal Ni-base superalloy during creep. The temperature difference between the alloy's aging condition and the creep-experiment temperature drives a creep-induced partitioning flux, causing elements to redistribute within the γ' phase and accumulate at planar faults. In this work, the single-crystal Ni-base superalloy ERBO-1 (SX) was creep-deformed using double-shear creep testing at 250 MPa and 750 °C, which is 120 °C below the preceding aging treatment temperature. At 1 and 2 pct strain, the interrupted creep states show planar faults with solute segregation as commonly observed in this low-temperature, high-stress regime. Solute segregation at superlattice extrinsic stacking faults (SESF), anti-phase boundaries (APB), and microtwins in the γ' phase reveals systematic depletion of Ni and Al, accompanied by enrichment of Re, Co, Cr, Mo, and Ti. Thermodynamic calculations predict the temperature-dependent γ/γ' compositions. Under the present experimental conditions, this results in increased uptake of Ni and Al and rejection of Re, Co, and Cr by the γ' phase. Consequently, depletion of Ni and Al and enrichment of Re, Co, and Cr are detected at planar defect sites. In contrast, Ti, Mo, Ta, and W segregation at microtwins and SESFs cannot be explained by bulk γ' partitioning and is instead attributed to localized phase transformations in the vicinity of the defects.

https://doi.org/10.1007/s11661-026-08173-4

I. INTRODUCTION

NI-BASE single-crystal superalloys are widely used for turbine blade applications and represent complex high-temperature materials containing up to ten alloying elements.[1] During service, these alloys must withstand high mechanical loads at elevated temperatures, which leads to creep deformation. Their excellent performance relies on a characteristic two-phase microstructure consisting of cuboidal γ' precipitates ($L1_2$ crystal structure) embedded in a face-centered cubic γ matrix.

Creep deformation in single-crystal superalloys involves dislocation glide within γ channels as well as dislocation shearing of γ' precipitates, which results in the formation of planar faults inside the γ' phase. The dominant deformation mechanisms strongly depend on temperature and applied stress.[1–3] Solute segregation occurs when alloying elements preferentially enrich or deplete at specific defect sites, eventually establishing a local chemical composition that resembles a steady-state concentration distinct from that of the surrounding bulk phase. Such defect-associated compositions are often referred to as "local defect phases."[4,5]

Solute atoms tend to migrate toward dislocations because dislocations locally distort the crystal lattice. This redistribution results in an equilibrium solute atmosphere, in which larger atoms preferentially occupy regions under tensile strain, while smaller atoms segregate to compressed regions.[6–8] This solute cloud surrounding the core of an edge dislocation is commonly referred to as a Cottrell atmosphere and can reduce local internal stresses by modifying dislocation energy and mobility.[8] In addition, Suzuki segregation to stacking faults reduces their fault energy by altering the local chemical composition.[9] Because the interaction energy of a solute atom at a stacking fault differs from that in

ZHONGMIN LONG, LUKAS GRÜNEWALD, and YOLITA M. EGGELER are with the Laboratory for Electron Microscopy, Karlsruhe Institute of Technology, Karlsruhe 76131, Baden-Württemberg, Germany. Contact e-mail: yolita.eggeler@kit.edu DAVID BÜRGER is with the Institute for Materials, Ruhr University Bochum, Bochum 44801, Nordrhein-Westfalen, Germany. VAMSHI KRISHNA RAO and K.V. VAMSI are with the Metallurgical Engineering and Materials Science, Indian Institute of Technology Indore, Indore 453552, India.

Manuscript submitted September 30, 2025; accepted February 15, 2026.
Article published online April 10, 2026

the perfect lattice, the equilibrium solute concentration within the fault differs from that of the surrounding bulk phase.[8,9]

Understanding solute segregation at various planar faults is essential for the design of next-generation superalloys with improved mechanical properties.[3] Segregation to planar faults lowers fault energies and facilitates continued dislocation shearing of γ' precipitates,[10,11] which constitutes a diffusion-controlled plastic deformation mechanism.

The segregation elements such as Co, Cr, W, Mo, Ta, Ti, and Nb at superlattice intrinsic stacking faults (SISF), superlattice extrinsic stacking faults (SESF) or anti-phase boundaries (APB) result in χ or η phase strengthening effects on single crystal (SX) superalloys, with their prototypes being Co_3 (W, Mo, Nb, Cr) or Ni_3(Ti, Mo, Nb, Ta).[12–16] Microtwin boundaries also exhibit local χ phase strengthening transformations.[17,18] For single SISF or SESF, non-χ or non-η phase formers may not be driven by local phase transformation but influenced by external factors. We propose that, when deformation occurs at a temperature lower than the final aging treatment temperature, SX superalloys attempt to re-establish a low-temperature thermodynamic equilibrium by redistributing partitioning preferences in the γ' phase.[19,20] Thus, these enriched non-χ or non-η phase elements might be driven by the re-establishment of phase equilibria as the temperature decreases.

To gain deeper insight into solute segregation of each alloying element along various planar faults, creep tests were performed at 750 °C and 250 MPa and interrupted at 1 pct and 2 pct creep strain with creep times of 13.2 and 35.5 hours, respectively. Qualitative comparisons using EDX maps post-processed by principal component analysis (PCA) and quantitative comparisons (based on composition changes) of the segregation tendencies of all alloying elements to planar defects help to understand how solute diffusion drives planar fault shearing.

II. EXPERIMENTAL

In the present study, the Re-containing SX superalloy ERBO-1 (CMSX-4 type) was creep-deformed using a double-shear creep testing technique at 750 °C and 250 MPa. The specimens were precisely oriented such that the macroscopic crystallographic shear system $(111)[11\bar{2}]$ is loaded during creep. All details concerning the alloys casting procedure and heat treatment of the superalloys and double-shear creep testing are given elsewhere.[21–24] The chemical composition of γ/γ' phases is listed in Table I.[21]

The samples were interrupted after reaching 1 and 2 pct plastic strains, respectively. TEM foils with $[1\bar{1}0]$ orientation were extracted from the crept samples, allowing edge-on observation of planar faults. The samples underwent mechanical grinding before being punched into disks with a 3 mm diameter and further fine ground to a thickness of approximately 80 to 100 μm. Subsequently, the disks were subjected to electro-chemical polishing using the commercial Struers A2 electrolyte at a temperature of − 18 °C and a voltage of 35 V to achieve electronic transparency.

The planar fault configurations were investigated using conventional transmission electron microscopy (TEM) with a Philips CM200, and high-resolution scanning transmission electron microscopy analysis (HRSTEM) and energy dispersive X-ray spectroscopy (EDXS) were performed using a high-angle annular dark field (HAADF) detector to generate Z contrast with a camera length of 91 mm on a probe-corrected Titan Themis Z operated at 300 kV. The Super-X detector is utilized to acquire EDXS maps with a screen current of approximately 80 pA and a beam convergence angle of 30 *mrad*. The image processing and geometry phase analysis (GPA) were carried out using the Velox software and Gatan Digital micrograph. The center of symmetry (COS) analysis[25,26] was executed to assess the Burgers vector of dislocations as well as the displacement vector of stacking faults by applying the finish to start right hand (FS/RH) convention.[27] The principle component analysis (PCA)[28] is employed to process the raw EDXS data in order to enhance the signal-to-noise ratio, thereby facilitating the generation of a more accurate elemental distribution map based on different intensity spectra and unbiasedly treating different regions as different main components. All the EDXS results were processed by PCA and presented as net intensity maps in Section III, and the chemical composition changes of segregated alloying elements are further quantitatively analyzed in Section IV.

III. RESULTS

A. *SESF and Microtwin Formation after 1 pct Creep*

The planar fault configuration of the SESF in the 1 pct crept sample that is partly transformed into a microtwin is characterized by TEM-bright-field (BF) and STEM-HAADF imaging, as presented in Figures 1 and 2. The entire fault terminates the shearing process within the γ' precipitate, exhibiting two distinct strain field alterations in the leading and central regions, as illustrated in Figure 1(a). The two lattice distortions exhibit bright diffraction contrast imaged by the HAADF detector with a high camera length of 140 mm in Figures 1(b) and (c) from the marked green and orange boxes, respectively. An increase in camera length allows for the inclusion of scattered electrons with low angles, which are typically used for annular dark field imaging. It can therefore be concluded that the bright contrast observed in Figures 1(b) and (c) with camera length of 140 mm is not solely attributable to the segregation of high atomic number elements for Z contrast, but also to the lattice distortion of planar faults for diffraction contrast. In Figure 1(b), the entire fault also leaves the trailing shearing trace in the γ channel. An additional independent planar fault is generated on the parallel (111) plane in the γ phase, as

Table I. Chemical Composition of γ and γ' Phases of ERBO-1C SX Superalloys Measured by STEM-EDX

Element	Al	Co	Cr	Hf	Mo	Re	Ta	Ti	W	Ni
γ (At. Pct)	2.62	20.41	22.19	0	0.88	5.12	0.13	0.14	4.06	44.45
γ' (At. Pct)	16.47	6.16	2	0.04	0.27	0.23	3.82	1.79	2.21	67.02

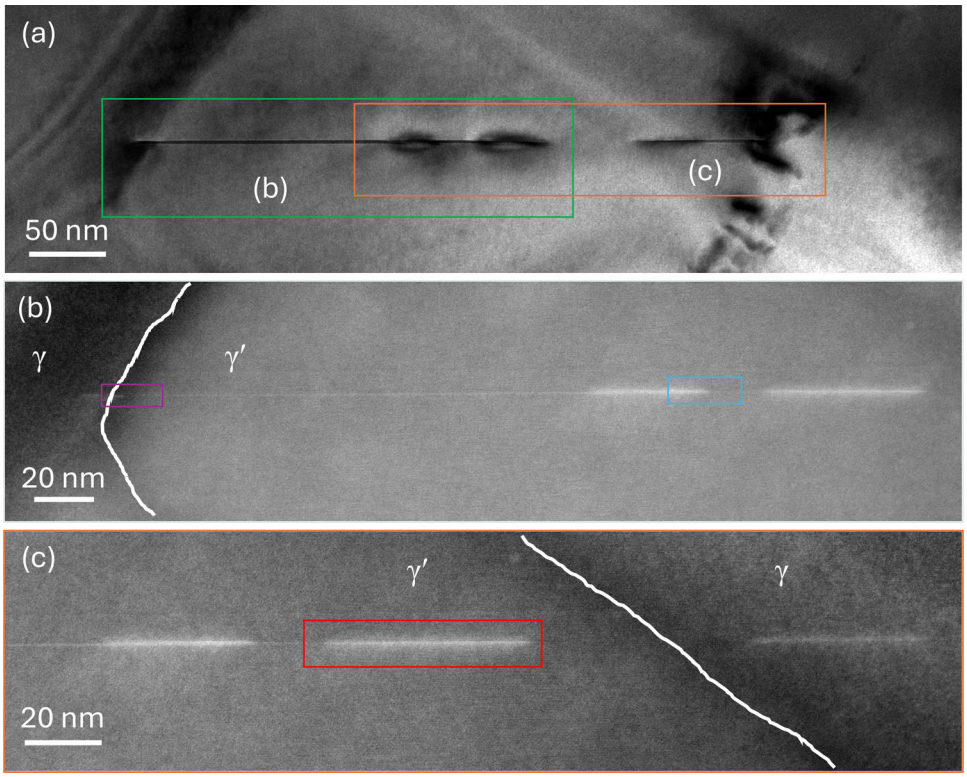

Fig. 1—The defect configuration of the SESF that is partly transformed into a microtwin: (*a*) TEM-BF micrograph presents two pronounced strain fields due to partial dislocations and fringe contrast of stacking faults, and the whole planar fault terminated shearing near the γ/γ' interface. (*b*) The low-magnification HAADF image taken from green box in (a) displays the entire fault is inside the γ' precipitate and further discussed in higher magnification in Figure 2. (*c*) The HAADF image taken from orange box in (a) presents the leading region of current fault configuration and an independent fault in the right γ channel.

exhibited in Figure 1(c). The marked purple, blue (Figure 1(b)), and red boxes (Figure 1(c)) in the two HAADF images, corresponding to the γ channel, the middle of the fault transition, and the leading regions of the complete fault configuration, are further investigated by high-resolution imaging and shown in Figure 2.

Figure 2 exhibits HR-HAADF micrographs and COS maps of the SESF that is partly transformed into a microtwin, showcasing the trailing microtwin, the transition region between SESF and microtwin, and the leading region of SESF. These images are derived from Figures 1(b) and (c) and provide a comprehensive visual representation of the microtwin and SESF characteristics. Figure 2(c) depicts the SESF generated by a pair of Shockley partials of $\frac{a}{6}[11\bar{2}]$ on adjacent (111) planes, as identified by the inverse fast Fourier transform (IFFT) image in Figure 3(a), where the two edge dislocations inserted from top left are observed. The Burgers circuit around the SESF tip shown in COS map in Figure 2(c) yields a shift of 0.28 nm for SESF with displacement vector of $\frac{a}{3}[11\bar{2}]$, which exactly corresponds to the two inserted edge dislocations. It can be inferred that a pair of dislocations with a Burgers vector of $\frac{a}{6}[11\bar{2}]$ shears through the ordered $L1_2$ crystal resulting in an unfavorable complex extrinsic stacking fault (CESF). This high energy CESF undergoes a reshuffling process to generate a stable SESF, a transition previously discussed and observed in Reference 13. This CESF configuration can be further sheared by additional partial dislocations with a Burgers vector of $\frac{a}{6}[11\bar{2}]$ to form a microtwin, a mechanism both predicted theoretically by Kolbe[29] and confirmed experimentally by Kovarik.[30] Figure 3(b) shows that two additional Shockley partial dislocations with a Burgers vector of $\frac{a}{6}[11\bar{2}]$ are introduced on above adjacent (111) planes. This dislocation shearing also follows reshuffling and transformation processes whereby the 2-layer microtwin of the SESF is transformed into a 4-layer microtwin with a displacement of 0.6 nm, as observed in the high-resolution HAADF

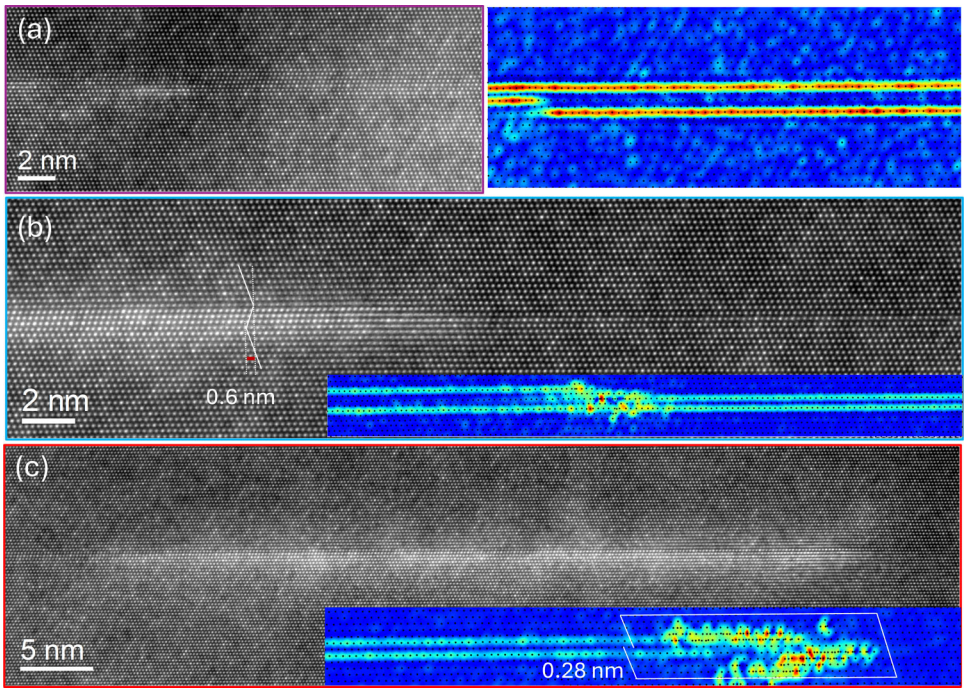

Fig. 2—The SESF that is partly transformed into a microtwin is analyzed by HR-HAADF micrographs and COS maps: (*a*) the trailing part of the microtwin is connected by an ESF in the γ channel. (*b*) Two additional lattice planes were sheared by Shockley partials to transform the SESF into a four-layer microtwin. (*c*) The SESF terminated shearing process inside γ' precipitate.

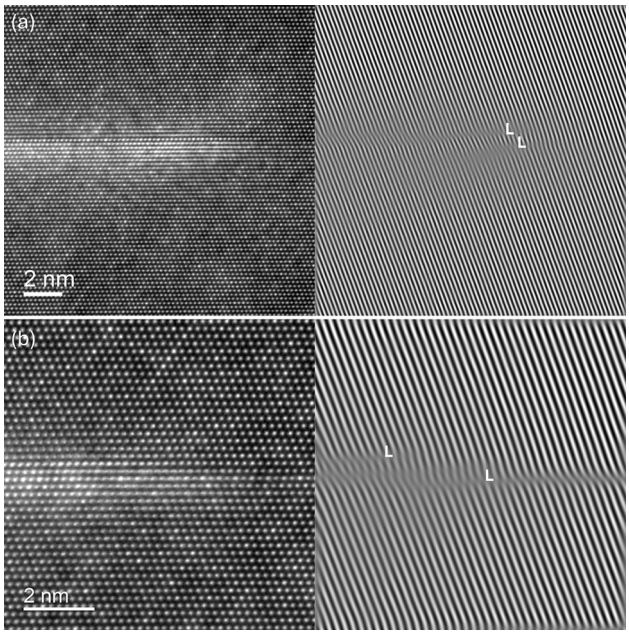

Fig. 3—HR-HAADF micrographs and corresponding IFFT images obtained by reflection $\pm(11\bar{1})$ of microtwin/SESF configuration for 1 pct crept sample: (*a*) a pair of Shockley partial dislocations of $\frac{a}{6}[11\bar{2}]$ at SESF tip inserted from the top left. (*b*) Two additional Shockley partial dislocations of $\frac{a}{6}[11\bar{2}]$ are observed between the SESF and microtwin.

micrograph and corresponding inset COS map in Figure 2(b). The microtwin, which has been created, is connected to an ESF at the γ/γ' interface in Figure 2(a). The first pair of Shockley partials may initiate shearing the $L1_2$ phase from the γ/γ' interface, subsequently gliding into the precipitate. The second pair of Shockley dislocations cuts the γ matrix, generating an ESF, and continuously shears into the γ' phase on the additional adjacent (111) planes. This process ultimately leads to the formation of the microtwin. It can be observed that the SESF terminates shearing the γ' precipitate in Figure 2(c), the distorted lattice planes of which exhibit bright diffraction contrast in close proximity to the leading Shockley partials. This is due to the fact that the strain field is enlarged by the high camera length of 140 mm. In contrast, the subsequent SESF, which is situated at a far distance from the leading dislocations, does not exhibit such bright contrast. This experimental phenomenon is also observed in the case of microtwin, as shown in Figure 2(b). The region of microtwin closer to the partial dislocations gives brighter contrast.

Figure 4 presents the EDX results including the trailing part of the SESF, the second pair of partial dislocations, and the leading microtwin. They exhibit the identical segregation behavior of an enrichment with Co, Cr, Mo, Ti, and Re, while a depletion with Ta, Hf, Ni, and Al of γ' formers, with the exception of W, which is also depleted. Notably, a Cottrell atmosphere is absent in the vicinity of the second pair of partial dislocations, which transform the SESF into a microtwin. This also indicates that the partial dislocations may not be the only reason that drives Cottrell cloud. The concentration profiles across the microtwin and the SESF, shown in Figure 5, reveal that both planar faults are clearly enriched with Co, Cr, Re, Ti, and Ta, while being depleted in Ni and Al. In contrast, the remaining alloying elements of Hf and Mo do not exhibit

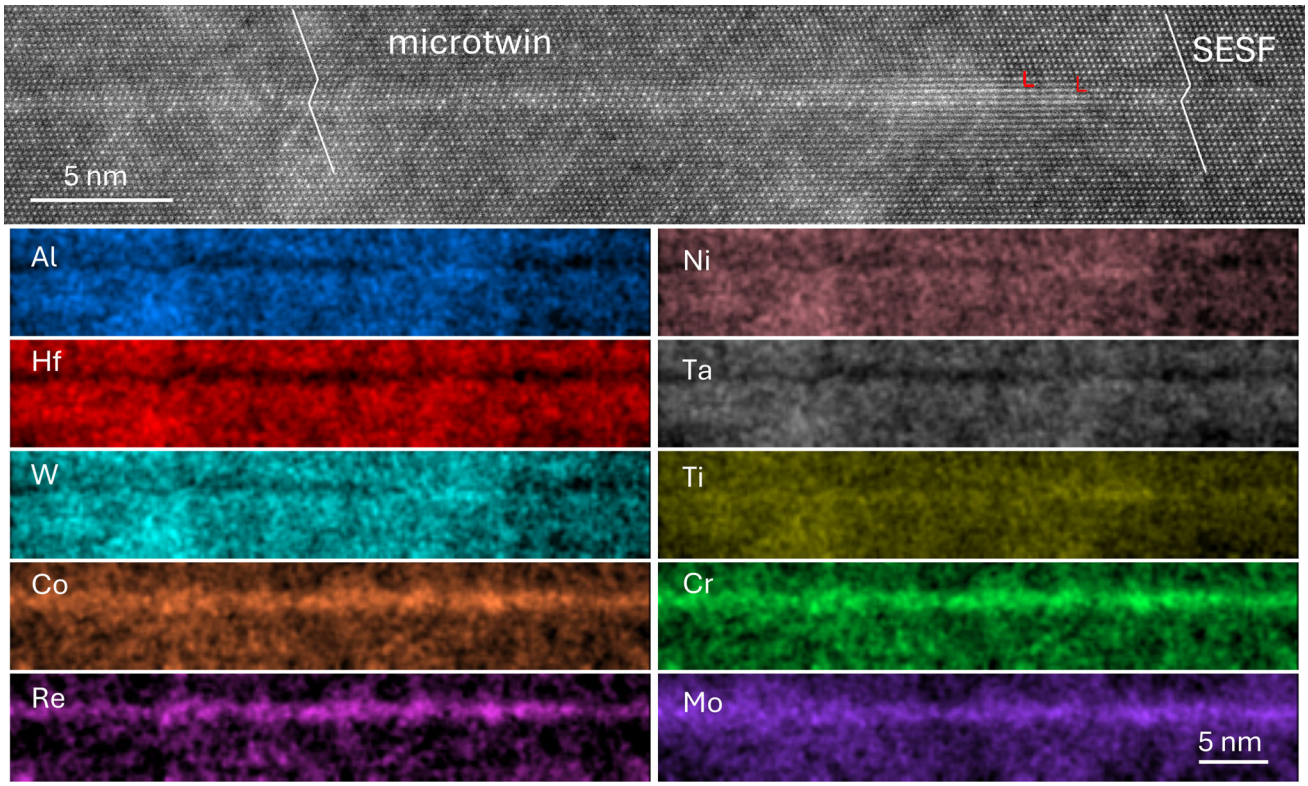

Fig. 4—The microtwin and a short SESF of the 1 pct crept sample including the transition between them are analyzed by EDX measurement. The net intensity EDX elemental maps are post-processed. The results demonstrate that the microtwin and SESF exhibit the identical segregation behavior of an enrichment with Co, Cr, Mo, Ti, and Re, while a depletion with Ta, Hf, Ni, and Al of γ' formers, with the exception of W, which is also depleted. The second pair of partial dislocations does not exhibit any Cottrell atmosphere.

pronounced segregation in the line scan profiles. This is primarily attributed to the limited signal-to-noise ratio of the EDX measurements, which hinders the reliable detection of subtle compositional variations. W also obviously enriches at microtwin while no fluctuation at SESF, which indicates that the enrichment of W tends to create the Co_3W along microtwin boundaries. Nevertheless, considering both the net intensity elemental maps in Figure 4 and the quantified concentration profiles in atomic percent, it can be inferred that the microtwin and SESF are enriched with Ti, Co, and Cr, with indications of weaker enrichment in Ta and Re, and are correspondingly depleted in Ni and Al.

B. *An Independent SESF and a SESF Partly Transformed into an APB of 2 pct Crept Sample*

The dark-field (DF) image with g(002) shown in Figure 6(a) reveals that the two planar faults with bright diffraction fringe contrast are vertically separated by a distance approximately 50 nm in the γ' precipitate along the shearing direction [11$\bar{2}$]. The below extended fault exhibiting a very distinct defect configuration compared to the 1 pct crept sample is further investigated. Figure 6(a) depicts the entire planar fault initiated shearing process from the left γ/γ' interface and continuously glided through the γ' precipitate till the leading partial dislocations encountered another γ/γ' interface along loading direction of [11$\bar{2}$]. To further analyze the nature of the specific fault, the three distinct regions delineated by the various color boxes were examined using HR-HAADF imaging and GPA. Within the loading direction [11$\bar{2}$], the fringe contrast increases into a larger thickness fringe, suggesting either the TEM foil thickness is increasing, or the nature of stacking fault is changing the fringe contrast.

All HR-HAADF images in the second row were subsequently analyzed by GPA with diffraction reflection of g($\bar{1}\bar{1}$1) and g(002), yielding strain field maps in various directions. The strain field maps in *yy* directions were selected to present the strain change due to planar fault evolution. The intensity bar in each strain map is indicative of the relative strain change based on the strain distribution in the perfect lattice. Figures 6(b) and (c) demonstrates an isolated SESF and the corresponding strain change along the SESF. Figure 6(d) presents two distinct planar faults with identical bright *Z* contrast, suggesting that the two planar faults possess identical elemental segregation. However, the strain map in Figure 6(e) provides detailed strain changes. The upper SESF maintains its nature throughout the entire cutting process, in contrast to the lower SESF, which is transferred into an APB by showing negative strain to no strain deviation, separated by a partial dislocation. Figure 7 further corroborates the distorted lattice planes for the entire upper SESF, while regarding the below fault that only the front SESF exhibits lattice distortion, and the behind APB displays perfect lattice planes. In

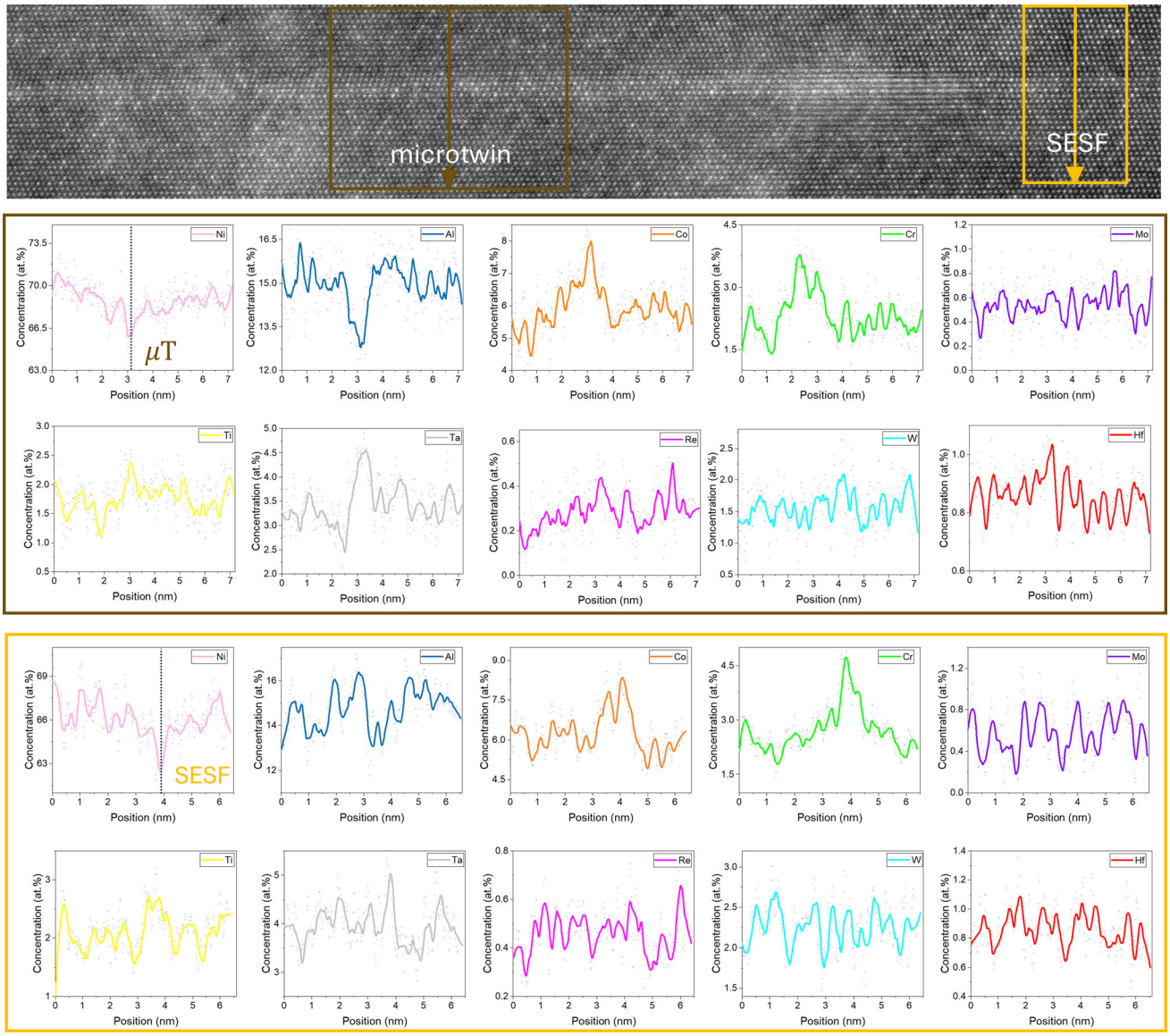

Fig. 5—The quantified concentration profiles across the microtwin and SESF of the 1 pct crept sample indicated in HAADF image. The line scan results are smoothed and the raw data are shown in gray dots. The line profiles indicate that across two different planar faults, i.e., microtwin and SESF, which are obviously enriched with Co, Cr, Re, Ti, and Ta, while depleted with Ni and Al. W also obviously enriches at microtwin while no fluctuation at SESF. The alloying elements of Hf and Mo do not show pronounced segregation.

addition, a half plane of a partial dislocation that inserted from the bottom between SESF and APB is observed. Figures 6(f) and (g) illustrate that the above SESF and below SESF along the shearing direction of $[11\bar{2}]$ continuously gliding on the (111) slip planes till the double-shear creep test was interrupted. Interestingly, leading dislocations within direction of $[\bar{1}\bar{1}2]$ initiated shearing γ channel and sheared into γ' precipitate, thereby creating a SISF.

However, the initiation shearing of APB is not directly observed, only the transition from SESF into APB is experimentally measured. The dislocation source of below planar fault formation might originate from the dissociation and cross slip of leading partial dislocation of the above SESF, or a dislocation loop expanding along two opposite directions $[11\bar{2}]$ and $[\bar{1}\bar{1}2]$. Further HRSTEM imaging is necessary for the trailing region of APB.

The chemical distribution in Figure 8 exhibits the elemental segregation to the middle regions of the independent SESF and the below SESF as well as the APB accompanied by a strain map. As Z contrast of the above SESF and the below SESF that is partly transformed into an APB shown in Figure 6(d), the net intensity EDX maps indicate that along above SESF, the γ formers of Mo, Co, Cr, W, and Re being enriched, while the γ' formers of Al, Ni, and Hf are depleted, with the exception of enriched Ti and Ta. Along the below SESF and transformed APB, W and Ta do not present pronounced segregation deviations while enriched with Ti. The quantified concentration profiles across the above independent SESF and transformed

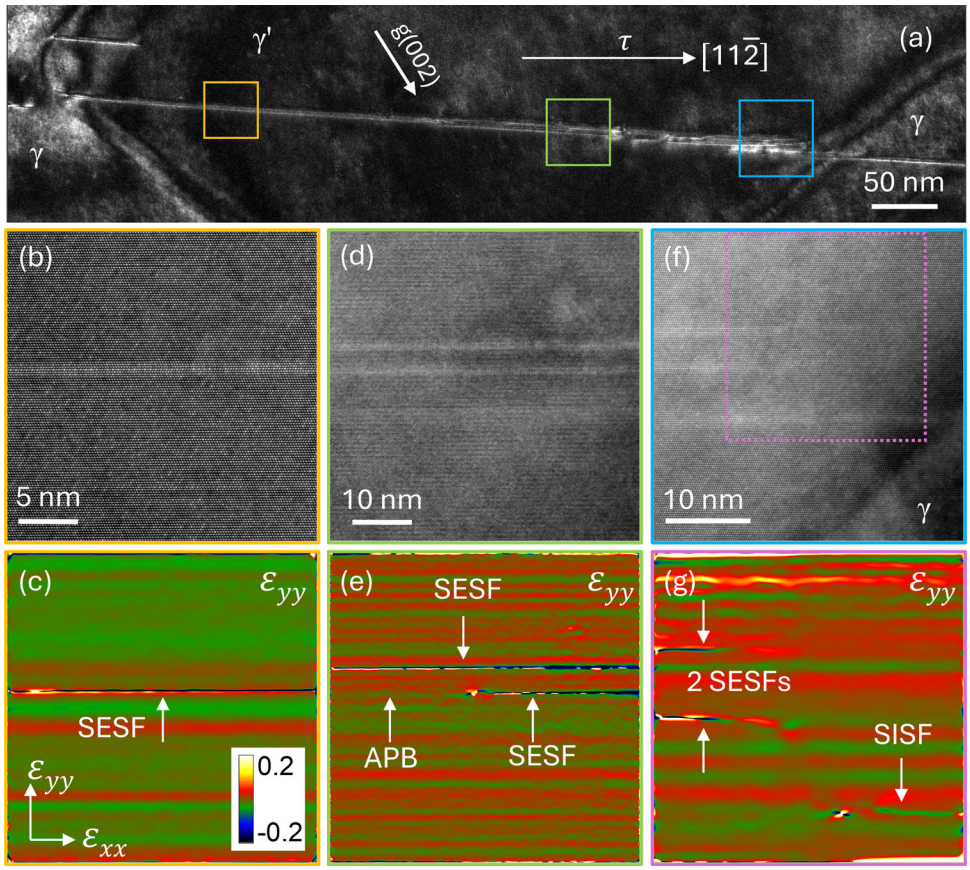

Fig. 6—(*a*) The below planar faults demonstrate that an independent SESF and another SESF on below slip plane that is partly transformed into an APB in the 2 pct crept sample. The HR-HAADF images in the middle row and the strain field maps in the third row are from the three marked different areas. The yellow area in (*b*) and (*c*) shows an isolated SESF. The green boxes in (*d*) and (*e*) present that two distinct faults separated by a distance of 5 nm. The blue area (*f*) and the pink dashed box (*g*) illustrate two SESFs that terminated shearing, and a SISF shears along [$\bar{1}\bar{1}$2] direction. All the strain maps are chosen from *yy* directions, and the intensity bar in (c) represents the relative strain change compared with perfect lattice planes (Color figure online).

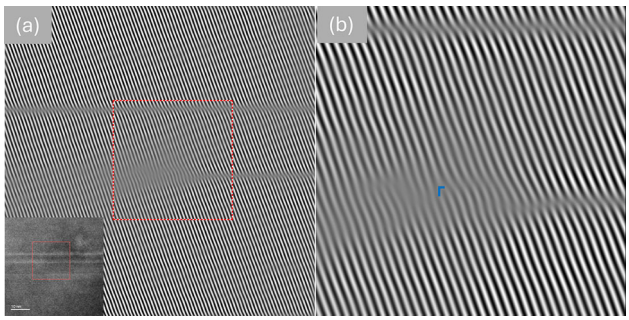

Fig. 7—(*a*) The IFFT image obtained by reflection ±(11$\bar{1}$) of middle region of the above SESF and the below SESF that is transformed into an APB from the marked area in the inset HRSTEM image. The upper SESF exhibits continuous distorted lattice planes. In contrast, the front SESF of the lower fault still presents strained lattice, while the rear APB exhibits no distortion. By zooming in the IFFT image to (*b*), a Shockley partial dislocation can be identified, inserted from the bottom between the transition APB and SESF.

APB presented in Figure 9 reveal that Ni and Al are depleted, while Co, Cr, and Re are enriched; W, Mo, Ta, and Hf do not show obvious segregation change for both faults. The Ti along the SESF still presents an enrichment, which can be attributed by the local η phase transformation to create Ni_3Ti.

IV. DISCUSSION

During high-temperature deformation of SX superalloys, the elemental segregation to stacking faults is considered as Suzuki locking,[9] further explained as local defect phase transformation according to the specific crystal structures of SFs and dislocations[4,5,12,13,17,31–33] or diffusion-assisted stacking fault lengthening.[10,14] As shown in the present work, the material system attempts to establish a new compositional steady state of the γ/γ' phases in response to changes in temperature by redistributing elemental partitioning preferences. When a specimen with a final aging temperature of 870 °C for 16 h is subjected to a creep temperature of 750 °C (creep times of 13.2 h (1 pct) and 35.5 h (2 pct)), in the γ' phase, solute atoms of Co, Cr, and Re are no longer tolerated, whereas Ni, Al, Ta, Ti, and W are increased. These changes in partitioning preference (cyan bars) are supported by MAT-Calc simulated results which have been published

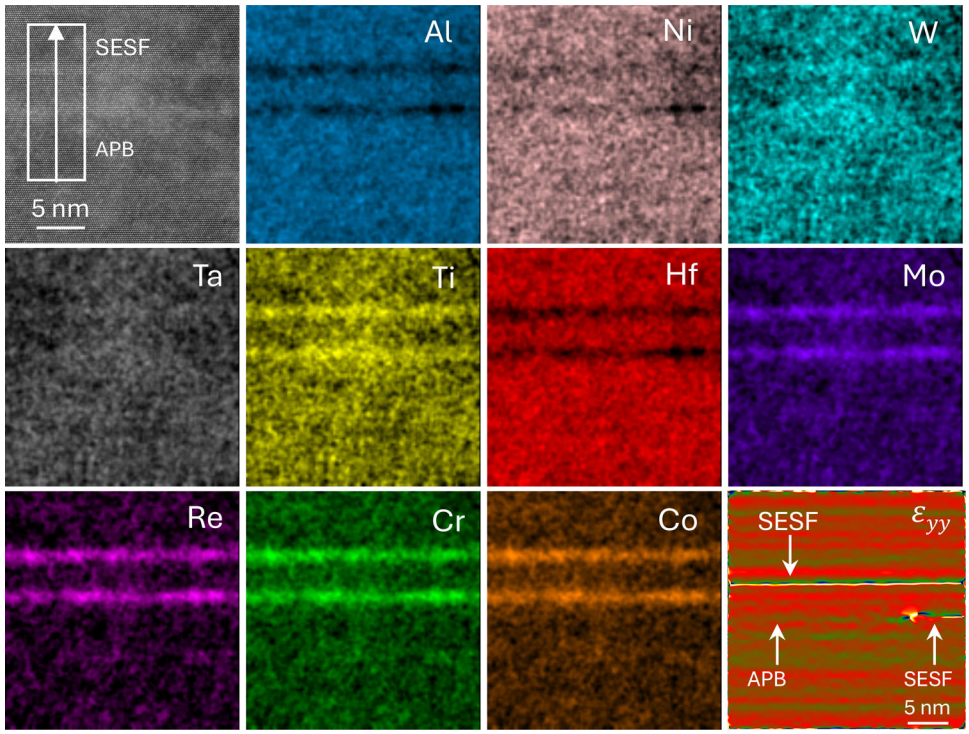

Fig. 8—The chemical distribution of the middle regions of independent SESF and the below SESF as well as the APB: the HRSTEM image and the corresponding net intensity EDX elemental maps of the middle SESF and SESF/APB along with their strain map of 2 pct crept sample. The results indicate that the two distinct planar faults exhibit identical elemental segregation, with the γ formers of Mo, Co, Cr, W, and Re being enriched, while the γ' formers of Al, Ni, and Hf are depleted, with the exception of enriched Ti [this EDX measurement area corresponds to the green box in Fig. 6(a)].

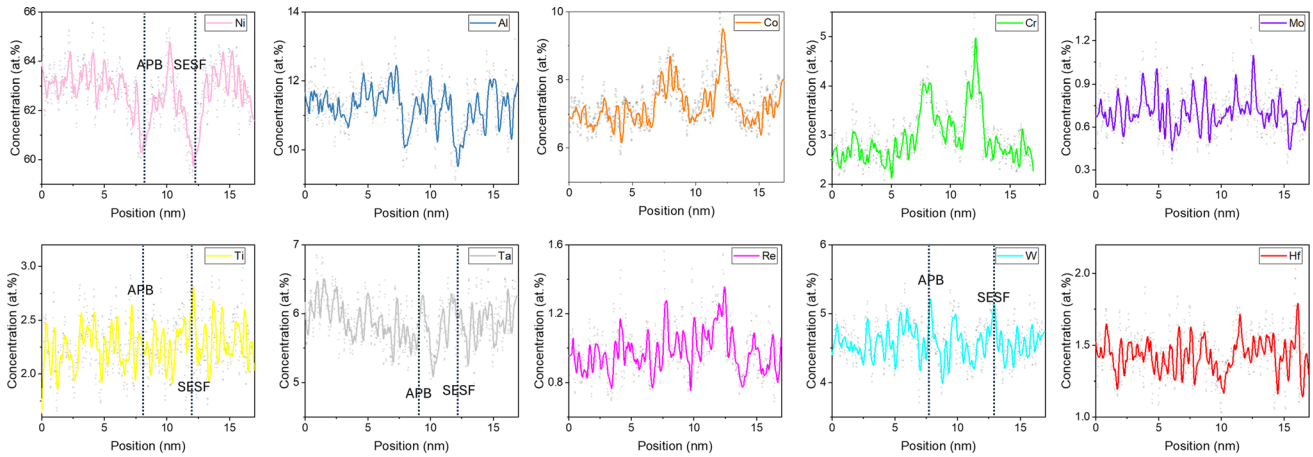

Fig. 9—The quantified concentration profiles across the above independent SESF and transformed APB as indicated in HAADF image in Fig. 8. The line scan results are smoothed and the raw data are shown in gray dots. The line profiles present that of the 2 pct crept sample Ni and Al are depleted, while Co, Cr, and Re are enriched, W, Mo, Ta, and Hf do not show obvious segregation change for both faults. The Ti along the SESF presents an enrichment.

elsewhere[19] and are reused with permission for comparison here (Figure 10).

Moreover, the quantified chemical compositions of segregated elements along SESFs, microtwins, and APBs of 1 and 2 pct crept samples are quantitatively normalized by their own γ' concentration of each alloying element, (compare Figure 10). Interestingly, the quantified elemental composition changes of Ta and Ti along SESF and microtwin in 1 pct crept sample present that they are enriched as shown in concentration profiles in Figure 5, which is opposite with intensity EDX maps post-processed by PCA shown in Figure 4. The elements Co and W are commonly enriched along stacking faults, and they are considered as χ phase formers by creating a prototype of Co_3W with $D0_{19}$ crystal structure with a prototype Co_3W for

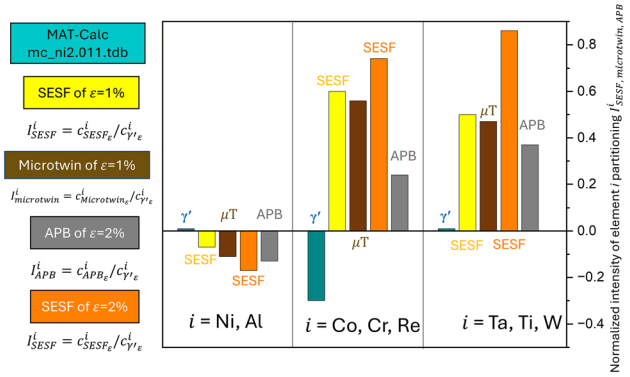

Fig. 10—The segregation behavior of planar faults was investigated and compared with simulation results of partitioning preference changes obtained by MAT-Calc (database mc-ni2.011.tdb). These simulation results are represented by the moderate cyan bar.[19] The remaining experimental data show the elemental segregation concentration along the SESF (yellow bar) and the microtwin (brown bar) in the 1 pct crept sample, as well as the SESF (yellow bar) and APB (gray bar) segregation in the 2 pct crept sample. All experimental data are normalized by the sample's own γ' composition and represent the normalized intensity of element i partitioning preference evolutions (Color figure online).

SISF.[11,34,35] The enrichment of Ti, Mo, and Ta can contribute to form $D0_{24}$ crystal structure with prototype of Ni_3Ti for SESF.[36–38] Figure 10 quantitatively presents the segregated elements at SESFs, microtwins, and APBs of 1 and 2 pct crept samples. In combination with qualitative intensity EDX maps in Figures 4 and 8 as well as concentration profiles across each fault in Figure 5 and 9, the results exhibit that along all planar faults, alloying elements of Ni and Al are depleted, while Co, Cr, and Re are enriched no matter what shear formation processes they possess. The segregation of alloying elements Ni, Al, Co, Cr, and Re continues to follow their usual partitioning preference behaviors in γ' phase as the material is subjected to a lower creep temperature than the final treatment temperature. Concerning the segregation of alloying elements of Ta, Ti, and W, along the microtwin and SESF in 1 pct crept sample as well as the above SESF in 2 pct, Ti and W shows an enrichment in both intensity maps and concentration profiles. This indicates that the SESFs in both sample tend to be locally transformed into a η phase by forming Ni_3Ti. Moreover, the inconsistency segregation of W and Ta along the microtwin in elemental map and concentration profiles indicates that the solute segregation of these two alloying elements to microtwin tends to locally form χ phase with Co_3W along the microtwin boundaries.

Among all elemental segregation to the observed planar faults in both samples, the only independent SESF which exhibits discernible local η phase transformation. This was found in the 2 pct sample either from qualitatively intensity EDX maps or quantitatively chemical compositional analysis. The transformation is accompanied with enrichment of Mo, W, Ta, and Ti in the formation of η phase with Ni_3Ti. The quantified SESF as well as transformed microtwin segregation in 1 pct crept sample also indicates that the local ordered phase transformations have created an η phase ($D0_{24}$, Ni_3Ti-type) at SESF and a χ phase ($D0_{19}$, Co_3W-type) at microtwin boundaries as demonstrated in References 17 and 18. In depleted Al zones W and Ti are enriched while Ni is replaced by Co, this facilitates local η and χ phases transformation.

In contrast, APB showing no γ' lattice shift and hence no local hexagonal crystals structure like the SESF, but are also enriched with Mo and Ti, does not demonstrate that APB undergoes a local phase transformation. Figures 8 and 10 reveal that APB shows almost identical elemental segregation tendencies like other planar faults in the present study. The elemental segregation to APBs[39,40] and in situ heating experiment[11] exhibit that APBs migrate away from the {111} planes into an energetically favorable cubic {001} planes to minimize fault energy through elemental segregation. This is because the APB energy on {001} is lower than its energy on {111} planes.[41–43] This migration behavior is not observed in the present work which, might be connected with the low creep temperature.

Moreover, the continuous shearing of trailing partial dislocations transforms the SESF into a microtwin and an APB in both samples. These trailing partial dislocations, which are inserted from either the top or bottom, all introduce high internal local stress fields compared to the perfect lattice planes shown in Figures 3 and 7, respectively. However, a high concentration of the Cottrell atmosphere is not observed experimentally around these inserted edge partial dislocations. This indicates partial dislocations might not drive Cottrell cloud formation.

All these elements are not regarded as ordered phase formers but still have enriched at APB. Their segregation can be driven by the establishment of a new thermodynamic equilibrium of the γ' phase due to new partitioning preferences of all elements. For instance, the independent SESF on the above slip planes in 2 pct crept sample exhibits depletion of Ni and Al, while Co, Cr and Re are enriched. These are exactly the alloying elements which the γ' phase attempts to take up (Ni and Al) or are no longer tolerated (Co, Cr, and Re). Despite the tendency of the γ' phase to occupy more of W, Ti, and Ta, these elements are still enriched at SESFs and microtwins to promote η or χ phase formations.

V. CONCLUSION

The elemental segregation at SESF, APB, and microtwin is evaluated in the superalloy ERBO-1, after creep deformation at 750 °C and 250 MPa. A comparative analysis of segregation of each alloying element in relation to various planar faults reveals that the creep deformation-induced planar faults in the γ' phase serve as preferential sites for solute segregation. This phenomenon occurs due to the re-establishment of low-temperature γ' phase thermodynamic equilibrium. Subsequently, the distinct atomic structures of SESF and microtwin boundaries drive distinct local composition to facilitate η and χ phase formations, respectively. In most cases, the SESF and microtwin segregation in

both samples are driven by both of the aforementioned reasons. In contrast, the elemental segregation to the APB is more dependent on the re-establishment of new phase equilibria through redistribution partitioning preferences in the γ' as temperature decreases rather than local phase transformation. This indicates that the redistribution partitioning preferences in the γ' phase play an important role for segregation behavior to establish a low-temperature compositional steady state and subsequently following the distinct crystal structure of specific stacking faults.

ACKNOWLEDGMENTS

The authors gratefully acknowledge financial support by the German Research Foundation (Deutsche Forschungsgemeinschaft, DFG), the Research Training Group GRK 2561 MatCom – ComMat, and Karlsruhe Nano Micro Facility (KNMFi) at Karlsruhe Institute of Technology for the access to probe-corrected Titan Themis Z. D. Bürger gratefully acknowledges funding through project A2 (No. 190389738) of the collaborative research center SFB/TR 103. K. V. Vamsi gratefully acknowledges IIT Indore for providing the Young Faculty Research Seed Grant (YFRSG). Z. Long and Y. M. Eggeler thank Dr. Malte Lenz and Nicolas Karpstein for center of symmetry script.

FUNDING

Open Access funding enabled and organized by Projekt DEAL.

CONFLICT OF INTEREST

On behalf of all authors, the corresponding author states that there is no conflict of interest.

OPEN ACCESS

REFERENCES

1. R.C. Reed: *The Superalloys: Fundamentals and Applications*, Cambridge University Press, Cambridge, 2006.
2. T.M. Pollock and S. Tin: *J. Propul. Power*, 2006, vol. 22(2), pp. 361–74. https://doi.org/10.2514/1.18239.
3. Y.M. Eggeler, K.V. Vamsi, and T.M. Pollock: *Annu. Rev. Mater. Res.*, 2021, vol. 51(1), pp. 209–40. https://doi.org/10.1146/annurev-matsci-102419-011433.
4. S. Korte-Kerzel, T. Hickel, L. Huber, D. Raabe, S. Sandlöbes-Haut, M. Todorova, and J. Neugebauer: *Int. Mater. Rev.*, 2021, vol. 67(1), pp. 89–117. https://doi.org/10.1080/09506608.2021.1930734.
5. P. Kontis and T.M. Smith: *Metall. Mater. Trans. A*, 2024, vol. 55A(12), pp. 4723–41. https://doi.org/10.1007/s11661-024-07626-y.
6. A.H. Cottrell and B.A. Bilby: *Proc. Phys. Soc. Lond. Sect. A*, 1949, vol. 62(1), p. 49. https://doi.org/10.1088/0370-1298/62/1/308.
7. A.H. Cottrell and M. Jaswon: *Proc. R. Soc. Lond. A*, 1949, vol. 199(1056), pp. 104–14.
8. H. Suzuki: *Sci. Rep. Res. Inst. Tohoku Univ. A*, 1952, vol. 4, pp. 455–63.
9. J.P. Hirth, J. Lothe, and T. Mura: *J. Appl. Mech.*, 1983, vol. 50(2), pp. 476–77.
10. D. Barba, T.M. Smith, J. Miao, M.J. Mills, and R.C. Reed: *Metall. Mater. Trans. A*, 2018, vol. 49A(9), pp. 4173–85. https://doi.org/10.1007/s11661-018-4567-6.
11. Y.M. Eggeler, J. Muller, M.S. Titus, A. Suzuki, T.M. Pollock, and E. Spiecker: *Acta Mater.*, 2016, vol. 113, pp. 335–49. https://doi.org/10.1016/j.actamat.2016.03.077.
12. T.M. Smith, B.D. Esser, N. Antolin, A. Carlsson, R.E.A. Williams, A. Wessman, T. Hanlon, H.L. Fraser, W. Windl, D.W. McComb, and M.J. Mills: *Nat. Commun.*, 2016, vol. 7(1), p. 13434. https://doi.org/10.1038/ncomms13434.
13. T.M. Smith, B.D. Esser, N. Antolin, G.B. Viswanathan, T. Hanlon, A. Wessman, D. Mourer, W. Windl, D.W. McComb, and M.J. Mills: *Acta Mater.*, 2015, vol. 100, pp. 19–31. https://doi.org/10.1016/j.actamat.2015.08.053.
14. T.M. Smith, B.D. Esser, B. Good, M.S. Hooshmand, G.B. Viswanathan, C.M.F. Rae, M. Ghazisaeidi, D.W. McComb, and M.J. Mills: *Metall. Mater. Trans. A*, 2018, vol. 49(9), pp. 4186–98. https://doi.org/10.1007/s11661-018-4701-5.
15. T.M. Smith, B.S. Good, T.P. Gabb, B.D. Esser, A.J. Egan, L.J. Evans, D.W. McComb, and M.J. Mills: *Acta Mater.*, 2019, vol. 172, pp. 55–65. https://doi.org/10.1016/j.actamat.2019.04.038.
16. T.M. Smith, N.A. Zarkevich, A.J. Egan, J. Stuckner, T.P. Gabb, J.W. Lawson, and M.J. Mills: *Commun. Mater.*, 2021, vol. 2(1), p. 106. https://doi.org/10.1038/s43246-021-00210-6.
17. A.J. Egan, F. Xue, Y. Rao, G. Sparks, E. Marquis, M. Ghazisaeidi, S. Tin, and M.J. Mills: *Acta Mater.*, 2022, vol. 238, p. 118206. https://doi.org/10.1016/j.actamat.2022.118206.
18. A.J. Egan, N.S.H. Gunda, L. Feng, M. Ghazisaeidi, Y. Wang, S. Tin, and M.J. Mills: *Commun. Mater.*, 2025, vol. 6(1), p. 180. https://doi.org/10.1038/s43246-025-00895-z.
19. V. Yardley, I. Povstugar, P.-P. Choi, D. Raabe, A.B. Parsa, A. Kostka, C. Somsen, A. Dlouhy, K. Neuking, E.P. George, and G. Eggeler: *Adv. Eng. Mater.*, 2016, vol. 18(9), pp. 1556–67. https://doi.org/10.1002/adem.201600237.
20. Y.M. Eggeler, D. Kubacka, P. Pichler, M. Wu, and E. Spiecker: *Scr. Mater.*, 2021, vol. 192, pp. 120–24. https://doi.org/10.1016/j.scriptamat.2020.10.002.
21. A.B. Parsa, P. Wollgramm, H. Buck, C. Somsen, A. Kostka, I. Povstugar, P.-P. Choi, D. Raabe, A. Dlouhy, J. Müller, E. Spiecker, K. Demtroder, J. Schreuer, K. Neuking, and G. Eggeler: *Adv. Eng. Mater.*, 2015, vol. 17(2), pp. 216–30. https://doi.org/10.1002/adem.201400136.
22. G. Eggeler, N. Wieczorek, F. Fox, S. Berglund, D. Bürger, A. Dlouhy, P. Wollgramm, K. Neuking, J. Schreuer, L. Agudo Jácome, S. Gao, A. Hartmaier, and G. Laplanche: *Metall. Mater. Trans. A*, 2018, vol. 49(9), pp. 3951–62. https://doi.org/10.1007/s11661-018-4726-9.
23. D. Bürger, A. Dlouhý, K. Yoshimi, and G. Eggeler: *Mater. Sci. Eng. A*, 2020, https://doi.org/10.1016/j.msea.2020.139961.
24. D. Bürger, A. Dlouhý, K. Yoshimi, and G. Eggeler: *Crystals*, 2023, vol. 10(2), p. 134. https://doi.org/10.3390/cryst10020134.
25. J. Li: Central symmetry parameter 2003.

26. O.M. Messé, J.S. Barnard, E.J. Pickering, P.A. Midgley, and C.M.F. Rae: *Philos. Mag.*, 2014, vol. 94(10), pp. 1132–52. https://doi.org/10.1080/14786435.2013.878052.
27. D. Hull and D.J. Bacon: *Introduction to Dislocations*, 5th ed. Butterworth-Heinemann, Oxford, 2011.
28. L. Grünewald: Electron microscopic investigation of superconducting Fe- and Cu-based thin films. Thesis, Karlsruher Institut für Technologie (KIT). 2022. https://doi.org/10.5445/IR/1000149357.
29. M. Kolbe: *Mater. Sci. Eng. A*, 2001, vol. 319–321, pp. 383–87. https://doi.org/10.1016/S0921-5093(01)00944-3.
30. L. Kovarik, R.R. Unocic, J. Li, P. Sarosi, C. Shen, Y. Wang, and M.J. Mills: *Prog. Mater. Sci.*, 2009, vol. 54(6), pp. 839–73. https://doi.org/10.1016/j.pmatsci.2009.03.010.
31. A. Bezold, J. Vollhüter, N. Karpstein, M. Lenz, A.P.A. Subramanyam, C.H. Zenk, T. Hammerschmidt, E. Spiecker, M. Göken, and S. Neumeier: *Commun. Mater.*, 2024, vol. 5(1), p. 8. https://doi.org/10.1038/s43246-024-00447-x.
32. A. Bezold, A.J. Egan, J. Völkl, N. Karpstein, T. Gaag, E. Spiecker, M. Göken, M.J. Mills, and S. Neumeier: *Scr. Mater.*, 2025, vol. 254, p. 116312. https://doi.org/10.1016/j.scriptamat.2024.116312.
33. A. Godha, D. Das, P. Ghosal, and S.K. Makineni: *Acta Mater.*, 2024, vol. 281, p. 120360. https://doi.org/10.1016/j.actamat.2024.120360.
34. M.S. Titus, Y.M. Eggeler, A. Suzuki, and T.M. Pollock: *Acta Mater.*, 2015, vol. 82, pp. 530–39. https://doi.org/10.1016/j.actamat.2014.08.033.
35. N. Karpstein, G. Laplanche, A. Saksena, R. Zehl, A. Bezold, O.M. Horst, D. Bürger, A. Kostka, C. Zenk, S. Neumeier, B. Gault, A. Ludwig, S.G. Fries, and E. Spiecker: *Acta Mater.*, 2024, https://doi.org/10.1016/j.actamat.2024.120416.
36. L. Feng, A. Egan, F. Xue, E. Marquis, M.J. Mills, and Y. Wang: *MRS Commun.*, 2022, vol. 12(6), pp. 991–1001. https://doi.org/10.1557/s43579-022-00251-z.
37. L. Feng, S.B. Kannan, A. Egan, T. Smith, M.J. Mills, M. Ghazisaeidi, and Y. Wang: *Acta Mater.*, 2022, vol. 240, p. 118287. https://doi.org/10.1016/j.actamat.2022.118287.
38. G. Liu, X. Xiao, M. Véron, and S. Birosca: *Acta Mater.*, 2020, vol. 185, pp. 493–506. https://doi.org/10.1016/j.actamat.2019.12.038.
39. Y.M. Eggeler, M.S. Titus, A. Suzuki, and T.M. Pollock: *Acta Mater.*, 2014, vol. 77, pp. 352–59. https://doi.org/10.1016/j.actamat.2014.04.037.
40. M. Lenz, M. Wu, J. He, S.K. Makineni, B. Gault, D. Raabe, S. Neumeier, and E. Spiecker: Atomic structure and chemical composition of planar fault structures in co-base superalloys. In: Superalloys 2020: Proceedings of the 14th International Symposium on Superalloys, p. 920–28. Springer.
41. H.P. Karnthaler, E.T. Mühlbacher, and C. Rentenberger: *Acta Mater.*, 1996, vol. 44(2), pp. 547–60. https://doi.org/10.1016/1359-6454(95)00191-3.
42. P. Beauchamp, J. Douin, and P. Veyssière: *Philos. Mag. A*, 1987, vol. 55(5), pp. 565–81. https://doi.org/10.1080/01418618708214369.
43. K.V. Vamsi, M.A. Charpagne, and T.M. Pollock: *Scr. Mater.*, 2021, vol. 204, p. 114126. https://doi.org/10.1016/j.scriptamat.2021.114126.